The Astrophysical Journal, 779:50 (9pp), 2013 December 10 doi:10.1088/0004-637X/779/1/50

A MEASUREMENT OF THE TURBULENCE-DRIVEN DENSITY DISTRIBUTION IN A NON-STAR-FORMING MOLECULAR CLOUD

Adam Ginsburg[1,2], Christoph Federrath[3], and Jeremy Darling[1]
[1] CASA, University of Colorado, 389-UCB, Boulder, CO 80309, USA; Adam.G.Ginsburg@gmail.com
[2] European Southern Observatory, Karl-Schwarzschild-Strasse 2, D-85748 Garching bei München, Germany
[3] Monash Centre for Astrophysics, School of Mathematical Sciences, Monash University, Vic 3800, Australia
Received 2013 August 26; accepted 2013 September 27; published 2013 November 25

ABSTRACT

Molecular clouds are supersonically turbulent. This turbulence governs the initial mass function and the star formation rate. In order to understand the details of star formation, it is therefore essential to understand the properties of turbulence, in particular the probability distribution of density in turbulent clouds. We present H_2CO volume density measurements of a non-star-forming cloud along the line of sight toward W49A. We use these measurements in conjunction with total mass estimates from ^{13}CO to infer the shape of the density probability distribution function. This method is complementary to measurements of turbulence via the column density distribution and should be applicable to any molecular cloud with detected CO. We show that turbulence in this cloud is probably compressively driven, with a compressive-to-total Mach number ratio $b = \mathcal{M}_C/\mathcal{M} > 0.4$. We measure the standard deviation of the density distribution, constraining it to the range $1.5 < \sigma_s < 1.9$, assuming that the density is lognormally distributed. This measurement represents an essential input into star formation laws. The method of averaging over different excitation conditions to produce a model of emission from a turbulent cloud is generally applicable to optically thin line observations.

Key words: stars: formation – turbulence

Online-only material: color figures

1. INTRODUCTION

Nearly all gas in the interstellar medium is supersonically turbulent. The properties of this turbulence, most importantly the shape of the density probability distribution function (ρ-PDF), are essential for determining how star formation progresses. There are now predictive theories of star formation that include formulations of the initial mass function (IMF; Padoan & Nordlund 2002; Padoan et al. 2007; Hennebelle & Chabrier 2008, 2009, 2013; Chabrier & Hennebelle 2010; Elmegreen 2011; Hopkins 2012) and the star formation rate (SFR; Krumholz & McKee 2005; Hennebelle & Chabrier 2011; Padoan & Nordlund 2011; Krumholz et al. 2012; Federrath & Klessen 2012, 2013; Padoan et al. 2012). The distribution of stellar masses and the overall SFR depend critically on the ρ-PDF established by turbulence. It is therefore essential to measure the ρ-PDF in the molecular clouds that produce stars.

Recent works have used simulations to characterize the density distribution from different driving modes of turbulence (Federrath et al. 2008, 2009, 2010, 2011; Price et al. 2011; Federrath & Klessen 2013). These studies determined that there is a relation between the mode of turbulent driving and the width of the lognormal density distribution, with the lognormal width (variance) $\sigma_s^2 = \ln(1 + b^2\mathcal{M}^2(\beta/(\beta+1)))$, where $\beta = 2(\mathcal{M}_A/\mathcal{M})^2 = 2(c_s/v_A)^2$ with sound speed c_s and Alfvén speed v_A, and the logarithmic density contrast $s \equiv \ln(\rho/\rho_0)$ (Padoan & Nordlund 2011; Molina et al. 2012).

The parameter b describes the coupling between the density contrast and the Mach number (Federrath et al. 2008, 2010). A conceptual justification for the parameter is that for solenoidal (curly) driving, only one of the three available spatial directions is directly compressed (longitudinal waves) and thus $b = 1/3$. Under compressive (convergent or divergent) driving, the gas is compressed in all three spatial directions, which gives $b = 3/3 = 1$. Federrath et al. (2008, 2010) showed that simulations driven with these modes achieve b values consistent with this interpretation.

All of the above turbulence-based theories of star formation explicitly assume a lognormal form for the density probability distribution $P_V(s)$ of the gas. However, recent simulations (Kritsuk et al. 2007; Schmidt et al. 2009; Federrath et al. 2010; Konstandin et al. 2012; Federrath & Klessen 2013; Federrath 2013) and theoretical work (Hopkins 2013) have shown that the assumption of a lognormal distribution is often very poor; theoretical intermittent distributions and simulated ρ-PDF s deviate from lognormal by orders of magnitude at the extreme ends of the density distributions. Since these theories all involve an integral over the density probability distribution function (PDF), deviation from the lognormal distribution can drastically affect the overall predicted SFR (e.g., Cho & Kim 2011; Collins et al. 2012) and IMF. Note that the modifications to the ρ-PDF driven by gravitational collapse are unlikely to change the SFR or the IMF since gravitational overdensities have already separated from the turbulent flow that created them (Klessen et al. 2000; Kritsuk et al. 2011; Federrath & Klessen 2012, 2013). It is therefore crucial that studies of turbulence focus on clouds that are not yet dominated by gravitational collapse (such as the cloud selected for this study) in order to study the initial conditions of star formation.

While simulations are powerful probes of wide ranges of parameter space, no simulation to date is capable of including all of the physical processes and spatial scales relevant to turbulence and star formation. Observations are required to provide additional constraints on properties of interstellar turbulence and guide simulators toward the most useful conditions and processes. Brunt (2010), Kainulainen & Tan (2013), and Kainulainen et al. (2013) provide some of the first observational constraints on the mode of turbulent driving using extinction-derived column density distributions. They measure the parameter $b \approx 0.4$–0.5, indicating that there is a "natural" mix

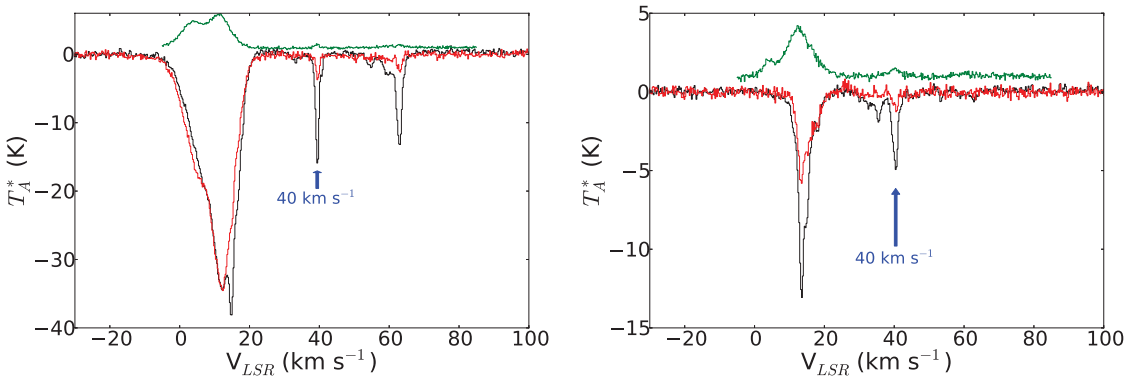

Figure 1. Spectra of the H_2CO 1_{10}–1_{11} (black), 2_{11}–2_{12} (red), and ^{13}CO 1–0 (green) lines toward G43.17+0.01 (left) and G43.16−0.03 (right). The H_2CO spectra are shown continuum-subtracted, and the ^{13}CO spectrum is offset by +1 K for clarity. The GBT 2_{11}–2_{12} spectra are multiplied by a factor of nine so the smaller lines can be seen. The blue arrow marks the 40 km s^{-1} cloud GRSMC 43.30-0.33 that we discuss in this paper.

(A color version of this figure is available in the online journal.)

of solenoidal and compressive modes. A "natural" mixture (a 2:1 mixture) of solenoidal and compressive modes injected by the turbulent driver, i.e., a forcing ratio $F_{\rm comp}/F_{\rm sol} = 1/2$, yields $b \sim 0.4$. Thus, $b > 0.4$ implies an enhanced compressive forcing component relative to the naturally mixed case (see Figure 8 in Federrath et al. 2010).

Formaldehyde, H_2CO, is a unique probe of density in molecular clouds (Mangum et al. 1993). Like CO, it is ubiquitous, with a nearly constant abundance wherever CO is found (Mangum & Wootten 1993; Tang et al. 2013). The lowest excitation transitions of o-H_2CO at 2 and 6 cm can be observed in absorption against the cosmic microwave background or any bright continuum source (Ginsburg et al. 2011; Darling & Zeiger 2012). The ratio of these lines is strongly sensitive to the local density of H_2, but it is relatively insensitive to the local gas temperature (Troscompt et al. 2009; Wiesenfeld & Faure 2013). The H_2CO line ratio has a direct dependence on the density that is nearly independent of the column density. This feature is unlike typical methods of molecular-line-based density inference in which the density is inferred to be greater than the critical density of the detected transition.

However, the particular property of the H_2CO densitometer we exploit here is its ability to trace the *mass-weighted* density of the gas. Typical density measurements from ^{13}CO or dust measure the total mass and assume a line-of-sight geometry, measuring a *volume-weighted* density, i.e., $\langle\rho\rangle_V = M_{\rm tot}/V_{\rm tot}$. In contrast, the H_2CO densitometer is sensitive to the density at which most mass resides; this fact will be demonstrated in greater detail in Section 4. The volume- and mass-weighted densities have different dependencies on the underlying density distributions, so in clouds dominated by turbulence, if we have measurements of both, we can constrain the shape of the ρ-PDF and potentially the driving mode.

In Ginsburg et al. (2011), we noted that the H_2CO densitometer revealed H_2 densities much higher than expected given the cloud-average densities from ^{13}CO observations. The densities were too high to be explained by a lognormal density distribution, consistent with that seen in local clouds. However, this argument was made on the basis of a statistical comparison of "cloud-average" versus H_2CO-derived density measurements and left open the possibility that we had selected particularly dense clouds. In this paper, we use the example of a single cloud to demonstrate that the high H_2CO densities must be caused by the shape of the density distribution and to infer the shape of this distribution.

Section 2 is a discussion of the observations used and the cloud selected for this study. Section 3 discusses the H_2CO line and the tools used to model it. Section 4 discusses the effect of turbulence on the H_2CO lines and the constraints our observations place on the gas density distribution.

2. OBSERVATIONS

We report H_2CO observations performed at the Arecibo Radio Observatory[4] and the Robert C. Byrd Green Bank Telescope (GBT)[5] that have been described in more detail in Ginsburg et al. (2011), with additional data to be published in a future work. The GBT observations were done in program GBT10B/019 and the Arecibo observations as part of project a2584. Arecibo and the GBT have FWHM $\approx 50''$ beams at the observed frequencies of 4.829 and 14.488 GHz, respectively. Observations were carried out in a single pointing position-switched mode with $3'$ and $5\farcm5$ offsets for the Arecibo and GBT observations, respectively; no absorption was found in the off position of the observations described here. The data were taken at 0.25 km s^{-1} resolution with 150 s on-source integrations for both lines. The continuum calibration uncertainty is $\sim$10%.

The Boston University/Five-College Radio Astronomy Observatory Galactic Ring Survey (GRS) ^{13}CO data was also used. The GRS (Jackson et al. 2006) is a survey of the Galactic plane in the ^{13}CO 1–0 line with $\sim 46''$ resolution. We used reduced data cubes of the $\ell = 43$ region.

2.1. GRSMC 43.30-0.33: A Non-star-forming Molecular Cloud

We examine the line of sight toward G43.17+0.01, also known as W49A. In a large survey, we observed two lines of sight toward W49, the second at G43.16−0.03. Both are very bright radio continuum sources, and two foreground giant molecular clouds (GMCs) are easily detected in both H_2CO absorption and ^{13}CO emission. Figure 1 shows the spectrum dominated by W49 itself, but with clear H_2CO foreground absorption components. The continuum levels subtracted from the spectra are 73 K at 6 cm and 11 K at 2 cm for the south component (G43.16−0.03),

[4] The Arecibo Observatory is operated by SRI International under a cooperative agreement with the National Science Foundation (AST-1100968), and in alliance with Ana G. Méndez-Universidad Metropolitana, and the Universities Space Research Association.

[5] The National Radio Astronomy Observatory is a facility of the National Science Foundation operated under cooperative agreement by Associated Universities, Inc.

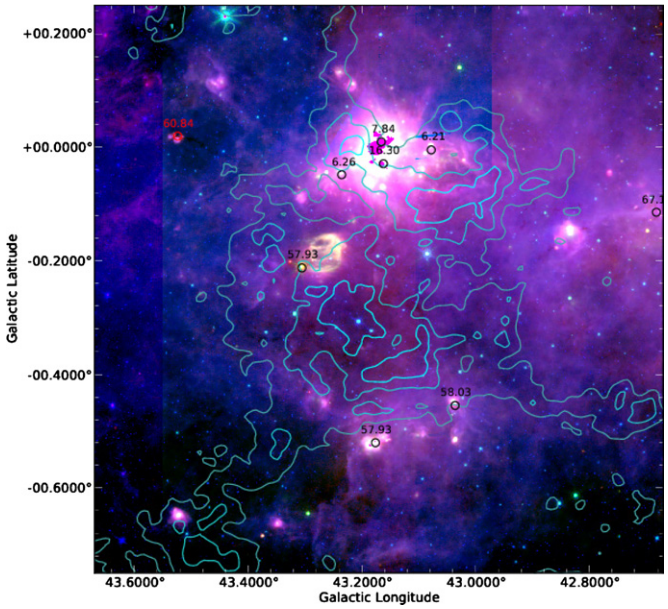

Figure 2. GRSMC 43.30–0.33 cloud. The background image shows *Herschel* SPIRE 70 μm (red), *Spitzer* MIPS 24 μm (green), and *Spitzer* IRAC 8 μm (blue) with the GRS ^{13}CO (Jackson et al. 2006) integrated image from $v_{\rm LSR} = 36$ km s^{-1} to $v_{\rm LSR} = 43$ km s^{-1} at contour levels of 1, 2, and 3 K km s^{-1} superposed in cyan contours. The red and black circles show the locations and beam sizes of the H_2CO observations, and their labels indicate the LSR velocity of the deepest absorption line in the spectrum. The W49 H II region is seen behind some of the faintest ^{13}CO emission. The dark swath in the 8 and 24 μm emission going through the peak of the ^{13}CO emission in the lower half of the image is a low optical depth infrared dark cloud associated with this cloud. The two pointings examined in this paper and shown in Figures 1 and 3 are labeled by their peak LSR velocities, 7.84 and 16.30, for G43.17+0.01 and G43.16−0.03, respectively. They are separated by about 1 pc at the distance to the 40 km s^{-1} cloud.

(A color version of this figure is available in the online journal.)

and 194 K at 6 cm and 28 K at 2 cm for the north component (G43.17+0.01).

We focus on the "foreground" line at ∼40 km s^{-1}, since it is not associated with the extremely massive W49 region, which is dominated by gravity and stellar feedback rather than pure turbulence. The cloud is shown in Figure 2. Additional H_2CO spectra of surrounding sources that are both bright at 8–1100 μm and within the ^{13}CO contours of the cloud have H_2CO 2_{11}–2_{12} detections at ∼10 or ∼60 km s^{-1}. The detections of dense gas at these other velocities, and corresponding nondetections of 2_{11}–2_{12} at 40 km s^{-1}, indicate that the star-forming clumps apparent in the infrared in Figure 2 are not associated with the 40 km s^{-1} cloud.

The H_2CO lines are observed in the outskirts of the cloud, not at the peak of the ^{13}CO emission. The cloud spans ∼0.°6, or ∼30 pc at $D = 2.8$ kpc (Roman-Duval et al. 2009). It is detected in 1_{10}–1_{11} absorption at all six locations observed in H_2CO (Figure 2), but 2_{11}–2_{12} is only detected in front of the W49 H II region because of the higher signal-to-noise ratio at that location. The detected ^{13}CO and H_2CO lines are fairly narrow, with H_2CO FWHM ranging from $\Delta v \sim 1.3$–2.8 km s^{-1} and ^{13}CO widths from $\Delta v \sim 1.5$–4.6 km s^{-1}, where the largest line widths are from averaging over the largest scales in the cloud. The ^{13}CO lines are 50%–100% wider than the H_2CO lines. This greater line width is due to high optical depth in the more common isotopologues, since C^{18}O has the same line width as H_2CO and ^{12}CO is 3× wider (Plume et al. 2004, their Table 4).

The highest ^{13}CO contours are observed as a modest infrared dark cloud in *Spitzer* 8 μm images, but no dust emission peaks are observed at 500 μm (*Herschel*; Traficante et al. 2011) or 1.1 mm (Bolocam; Aguirre et al. 2011; Ginsburg et al. 2013) associated with the dark gas. This is an indication that the cloud is not dominated by gravity—no massive dense clumps are present within this cloud.

The cloud's density is the key parameter we aim to measure, so we first determine the cloud-averaged properties based on ^{13}CO 1–0. The cloud has mass in the range $M_{\rm CO} = 1$–$3\times10^4\,M_\odot$ in a radius $r = 15$ pc as measured from the integrated ^{13}CO map using an optical depth estimate and abundance from Roman-Duval et al. (2010), so its mean density is $\rho(H_2) \approx 10$–30 cm^{-3}, assuming spherical symmetry (see the Appendix). If we instead assume a cubic volume, as is done in simulations, the mean density is lower by a factor $\pi/6$. Simon et al. (2001) report a mass $M_{\rm CO} = 6\times10^4\,M_\odot$ and $r = 13$ pc, yielding a density $\rho(H_2) = 100$ cm^{-3}, which is consistent with our estimates. Roman-Duval et al. (2010) break the cloud apart into three separate objects for their analysis, GRSMC 43.04-0.11, GRSMC 43.24-00.31, and GRSMC 43.14-0.36. All three have the same velocity to within 1 km s^{-1}, but they show slight discontinuities in position–velocity space. These discontinuities are morphologically consistent with gaps seen in turbulent simulations, validating our assessment of the cloud as a single object, but as a maximally conservative estimate we use the density of the northmost "clump" GRSMC 43.04-0.11, which overlaps our target line of sight, as an upper limit. It has density $\rho \approx 120$ cm^{-3}, but we use $\rho < 200$ cm^{-3} as a slightly more conservative limit to allow for modest uncertainties in optical depth, radius, and abundance.

3. MODELING H_2CO

In order to infer densities using the H_2CO densitometer, we use the low-temperature collision rates given by Troscompt et al. (2009)[6] with RADEX using the large velocity gradient (LVG) approximation (van der Tak et al. 2007) to build a grid of predicted line properties covering 100 densities $\rho(H_2) = 10 - 10^8$ cm^{-3}, 10 temperatures $T = 5$–50 K, 100 column densities N(o-H_2CO) $= 10^{11}$–10^{16}cm^{-2}, and 10 H_2 ortho-to-para ratios OPR = 0.001–3.0.

The H_2CO densitometer measurements are shown in Figure 3. The figures show optical depth spectra, given by the equation

$$\tau = -\ln\left(\frac{S_\nu + 2.73\,{\rm K}}{\bar{C}_\nu + 2.73\,{\rm K}}\right), \quad (1)$$

where S_ν is the spectrum (with both the line and continuum included) and $\bar{C}_\nu$ is the measured continuum, both in kelvin. The cosmic microwave background temperature is added to the continuum since H_2CO can be seen in absorption against it, though toward W49 it is negligible.

Since the W49 lines of sight are clearly on the outskirts of the foreground cloud, not through its center, it is unlikely that these lines of sight correspond to a centrally condensed density peak (e.g., a core). The comparable line ratios observed through two different lines of sight separated by ∼1 pc supports this claim, since if either line was centered on a core, we would observe a much higher 2_{11}–2_{12} optical depth.

[6] The Wiesenfeld & Faure (2013) rates provide access to higher temperatures, but for the low temperatures we are treating in this paper, the Troscompt et al. (2009) values are slightly more accurate (A. Faure 2013, private communication).

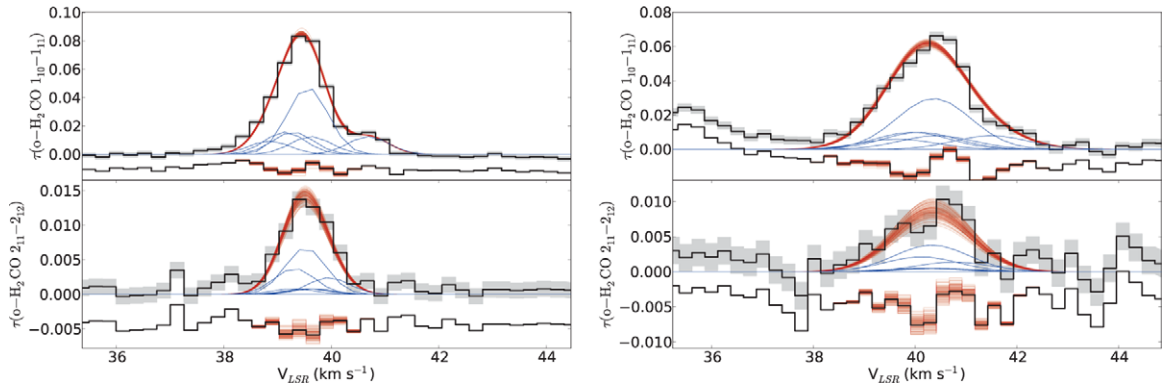

Figure 3. Optical depth spectra of the 1_{10}–1_{11} and 2_{11}–2_{12} lines toward the two W49 lines of sight, G43.17+0.01 (left) and G43.16−0.03 (right). The gray bars show the 1σ error bars on each data point. The red lines show 100 realizations from an MCMC fit of the o-H_2CO 1_{10}–1_{11} and 2_{11}–2_{12} lines using the LVG model grid. The blue lines show the hyperfine components that make up the 1_{10}–1_{11} and 2_{11}–2_{12} lines for the optimal fit; the 1_{10}–1_{11} line is resolved into two components in the G43.17+0.01 spectrum. The residuals of the fit are shown offset below the spectra with the residuals of the above 100 MCMC realizations overplotted in red. The optical depth ratio falls in a regime where gas temperature has very little effect on the observed depth and there is no degeneracy between low and high densities (Ginsburg et al. 2011).

(A color version of this figure is available in the online journal.)

Table 1
Fitted Parameters

	1_{10}–1_{11}	2_{11}–2_{12}
G43.17+0.01		
Centroid	$39.54^{+0.01}_{-0.01}$	$39.55^{+0.06}_{-0.06}$
Width	$0.37^{+0.01}_{-0.02}$	$0.45^{+0.07}_{-0.08}$
Peak	$0.114^{+0.004}_{-0.004}$	$0.015^{+0.002}_{-0.002}$
Integral	$0.107^{+0.002}_{-0.002}$	$0.016^{+0.002}_{-0.002}$
Ratio	$6.49^{+0.84}_{-0.67}$	
G43.16−0.03		
Centroid	$40.35^{+0.04}_{-0.03}$	$40.36^{+0.23}_{-0.22}$
Width	$0.72^{+0.04}_{-0.04}$	$0.84^{+0.23}_{-0.31}$
Peak	$0.071^{+0.003}_{-0.003}$	$0.008^{+0.002}_{-0.002}$
Integral	$0.130^{+0.005}_{-0.005}$	$0.018^{+0.004}_{-0.004}$
Ratio	$7.32^{+2.31}_{-1.43}$	

Notes. Centroid and width are in km s^{-1}, peak is unitless (optical depth), and the integral is in optical depth times km s^{-1}. The errors represent 95% credible intervals (2σ).

We performed fits of the optical depth spectra to each line independently using a Markov-Chain Monte Carlo (MCMC) approach (Ginsburg & Mirocha 2011; Patil et al. 2010). In both lines of sight, we found that the centroids and widths agreed (see Table 1).

Hereafter, we only discuss the G43.17+0.01 line of sight ($V_{\rm LSR} = 7.84$ km s^{-1} in Figure 2), since it is well-fit by a single component and has high signal-to-noise. Since both lines of sight sample the same CO cloud, all of the measurements below are most strongly constrained by the G43.17+0.01 line of sight and the G43.16−0.03 line of sight provides no additional information.

4. TURBULENCE AND THE H_2CO cm LINES

Supersonic interstellar turbulence can be characterized by its driving mode, Mach number $\mathcal{M}$, and magnetic field strength. We start by assuming that the gas density follows a lognormal distribution, defined as

$$P_V(s) = \frac{1}{\sqrt{2\pi\sigma_s^2}} \exp\left[-\frac{\left(s+\sigma_s^2/2\right)^2}{2\sigma_s^2}\right] \quad (2)$$

(Padoan & Nordlund 2011; Molina et al. 2012), where the subscript V indicates that this is a volume-weighted density distribution function. The parameter s is the logarithmic density contrast, $s \equiv \ln(\rho/\rho_0)$ for mean volume-averaged density $\rho_0 \equiv \langle\rho\rangle_V$. The width of the turbulent density distribution is given by

$$\sigma_s^2 = \ln\left(1 + b^2\mathcal{M}^2\frac{\beta}{\beta+1}\right), \quad (3)$$

where $\beta = 2c_s^2/v_A^2 = 2\mathcal{M}_A^2/\mathcal{M}^2$ and b ranges from $b \sim 1/3$ (solenoidal, divergence-free forcing) to $b \sim 1$ (compressive, curl-free) forcing (Federrath et al. 2008, 2010). c_s is the isothermal sound speed (s here is short for "sound"), v_A is the Alfvén speed, and $\mathcal{M}_A$ is the Alfvénic Mach number.

The observed H_2CO line ratio roughly depends on the *mass-weighted* PDF (as opposed to the volume-weighted distribution function, which is typically reported in simulations). For each H_2CO molecule, the likelihood of absorbing a background photon is set by the level population in the lower energy state, which is controlled by the H_2 density as long as the line is optically thin (which is the case we treat here).

For a given "cell" at density ρ, the optical depth is given by the number (or mass) of particles in that cell $M(\rho) = V \cdot \rho$ (assuming a fixed cell volume V) times the optical depth $\Upsilon_{\nu,p}$, where the subscript p indicates that this is an optical depth per particle. The total optical depth is the optical depth per cell integrated over the PDF, $\tau_{\rm tot} = \int M(\rho)\Upsilon_{\nu,p}P_V(\rho)d\rho$, which is equivalent to $\tau_{\rm tot} = \int \Upsilon_{\nu,p}P_M(\rho)d\rho$ using the definition of mass-weighted density $P_M(\rho) \equiv (\rho/\rho_0)P_V(\rho)$.

Following this derivation, we use the RADEX models of the H_2CO lines, which are computed assuming a fixed local density, as a starting point to model the observations of H_2CO in turbulence. Starting with a fixed *volume-averaged* density ρ_0, we compute the observed H_2CO optical depth τ_ν in both the 1_{10}–1_{11} and 2_{11}–2_{12} lines by averaging over the mass-weighted density distribution and redefining the equations with

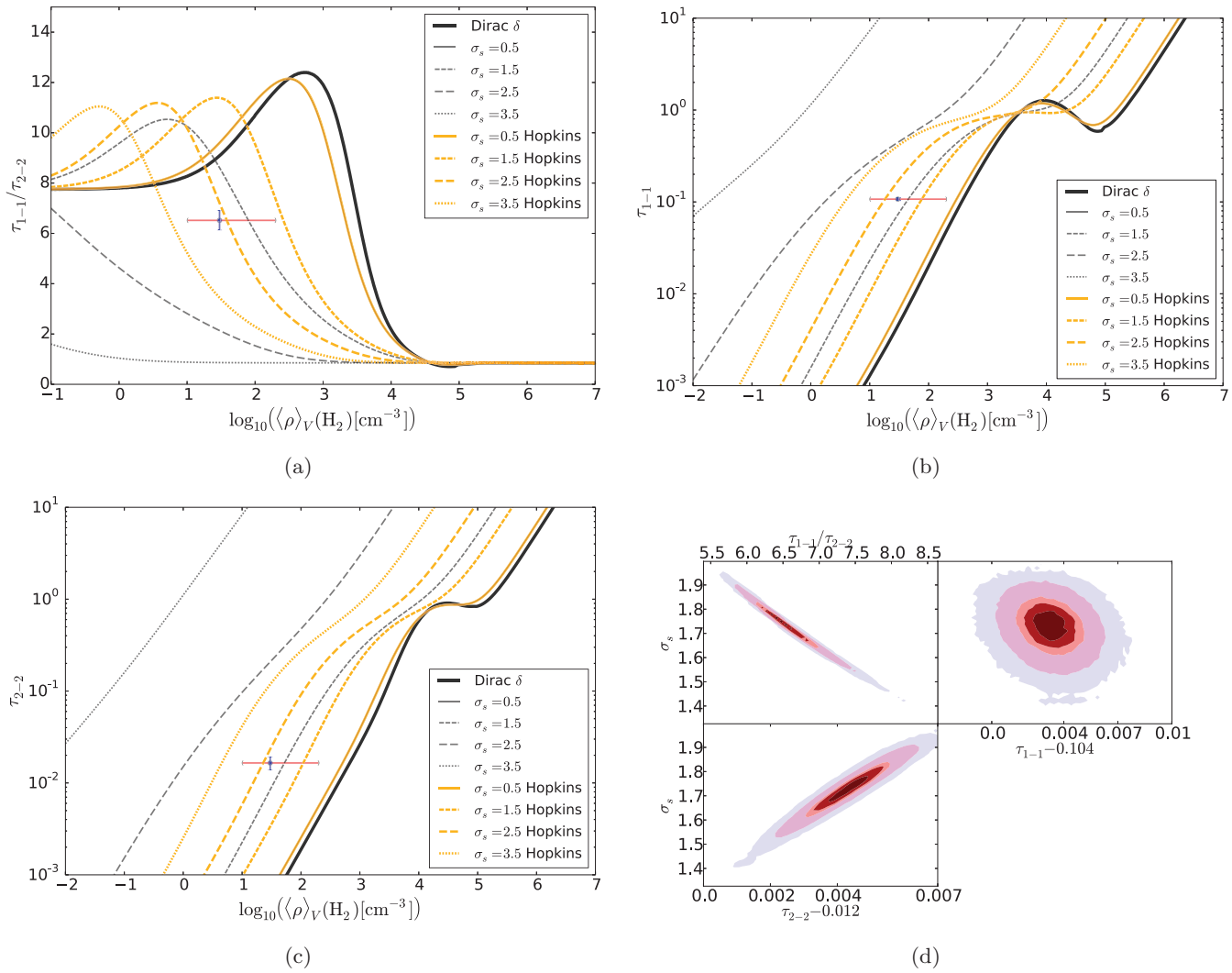

Figure 4. Predicted H_2CO 1_{10}–1_{11}/2_{11}–2_{12} ratio and optical depths as a function of the ^{13}CO-derived volume-weighted mean density for a fixed abundance relative to H_2 $X(\text{o-}H_2CO) = 10^{-8.5}$ with H_2 ortho/para ratio 1.0. The different lines show the effect of averaging over different mass distributions as identified in the legend. The thick solid line shows the predicted values with no averaging (i.e., a δ-function density distribution); the other solid line shows $\sigma_s = 0.5$ for both distributions (they overlap). The blue point shows the G43.17+0.01 measurement. The horizontal red error bars show the limits on the mean volume density, $\langle\rho\rangle_V$, and the vertical blue error bars show the 95% credible interval for the H_2CO line measurements. The bottom right panel shows the allowed σ_s parameter space for the lognormal distribution given the 1_{10}–1_{11} and 2_{11}–2_{12} measurements and their ratio; the values are reported in Table 2. The contours indicate the 25% (dark red), 50% (red), 68% (light red), 95% (pink), and 99.7% (blue-gray) credible regions.

(A color version of this figure is available in the online journal.)

a logarithmic differential:

$$\tau_\nu(\rho_0) = \int_{-\infty}^{\infty} \Upsilon_{\nu,p}(\rho) P_M(\ln \rho/\rho_0) d\ln(\rho/\rho_0) \quad (4)$$

$$= \int_{-\infty}^{\infty} \Upsilon_{\nu,p}(\rho_0 e^s) P_M(s) ds. \quad (5)$$

$\Upsilon_{\nu,p}(\rho)$ is the optical depth *per particle* at a given density, where N_p is the column density (per km s^{-1} pc^{-1}) from the LVG model. We assume a fixed abundance of o-H_2CO relative to H_2 (i.e., the H_2CO perfectly traces the H_2).[7]

[7] While there is building evidence that there is H_2 not traced by CO (Glover et al. 2010; Shetty et al. 2011a, 2011b), H_2CO abundances have typically been observed to be consistent with CO abundances, so the mass traced by the CO is the same we observe in H_2CO. H_2CO deficiency is also most likely to occur on the optically thin surfaces of clouds where the total gas density is expected to be lower, so our measurements should be largely unaffected by abundance variation within the cloud.

Figure 4 shows the result of this integral for an abundance of o-H_2CO relative to H_2, $X(\text{o-}H_2CO) = 10^{-8.5}$, where the X-axis shows the volume-averaged number density $\rho_0 \equiv \rho(H_2)$ and the Y-axis shows the observable optical depth ratio of the two H_2CO centimeter lines. The LVG model, which assumes a single density (or a Dirac δ function as the density distribution), is shown along with the PDF-weighted-average versions of the model that take into account realistic turbulent gas distributions.

The H_2CO 2_{11}–2_{12} line requires a higher density to be "refrigerated" into absorption. As a result, any spread of the density distribution means that a higher fraction of the mass is capable of exciting the 2_{11}–2_{12} line. Wider distributions increase the 2_{11}–2_{12} line more than the 1_{10}–1_{11} line and decrease the $(1_{10}$–$1_{11})/(2_{11}$–$2_{12})$ ratio.

4.1. The ρ-PDF in GRSMC 43.30-0.33

We use the density measurements in GRSMC 43.30-0.33 to infer properties of that cloud's density distribution. The observed

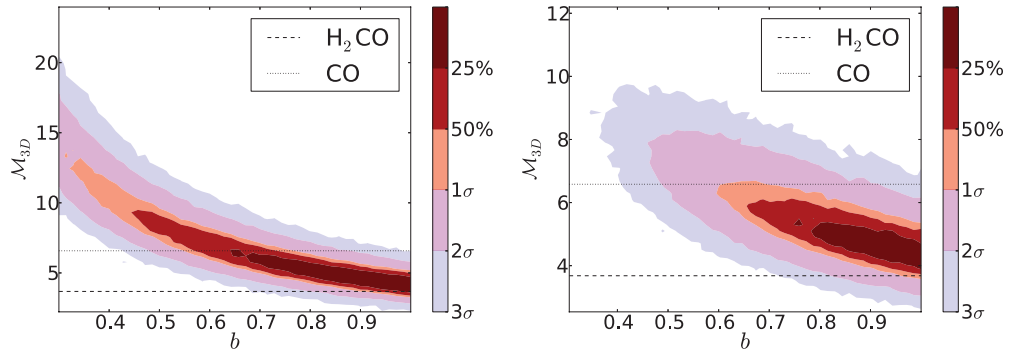

Figure 5. Contours of the MCMC fit to the H_2CO optical depths with the cloud mean density restricted to $10\,\mathrm{cm}^{-3} < \langle\rho\rangle_V < 200\,\mathrm{cm}^{-3}$. The contour levels indicate the regions in which 25%, 50%, 68%, 95%, and 99.7% of the MCMC samples are included. The left plot shows the parameter space allowed with no constraints on the Mach number, indicating the mild degeneracy between Mach and b. The right plot shows the parameters derived using the constraints on the Mach number based on the G43.17+0.01 line of sight, $\mathcal{M}_{3D} \approx 5.1 \pm 1.5$, which is half way between the value inferred from the H_2CO and ^{13}CO line widths. The horizontal lines in both plots represent the Mach numbers inferred from the H_2CO and CO line widths via Equation (6). Both plots are marginalized over the other free parameters (σ_s, ρ_V, and the observed optical depth).

(A color version of this figure is available in the online journal.)

Table 2
Fitted Distribution Parameters

Parameter	Lognormal	Hopkins
	$X(H_2CO) = 10^{-8.5}$	
σ_s	$1.7^{0.2}_{0.2}$	–
$\sigma_s \vert \mathcal{M}$	$1.7^{0.2}_{0.1}$	–
$b \vert \mathcal{M}$	>0.56	–
	$X(H_2CO) = 10^{-9.0}$	
σ_s	$1.5^{0.1}_{0.1}$	$2.7^{0.5}_{0.5}$
T	–	$0.31^{0.08}_{0.10}$
$\sigma_s \vert \mathcal{M}$	$1.5^{0.1}_{0.1}$	$2.5^{0.5}_{0.5}$
$T \vert \mathcal{M}$	–	$0.29^{0.08}_{0.08}$
$b \vert \mathcal{M}$	>0.41	>0.71

Notes. The error bars represent 95% credible intervals. For the b parameter, only the lower limit is shown. The $\vert\mathcal{M}$ notation indicates that the parameter measurement includes the constraints imposed by the Mach number measurements, for which we have adopted $\mathcal{M}_{3D} = 5.1 \pm 1.5$, where $\sigma_{\mathcal{M}} = 1.5$ is the standard deviation of the normal distribution we used to represent the Mach number. The –'s indicate disallowed parameter space (top) or parameters that are not part of the distribution (bottom).

line ratio for the G43.17+0.01 sightline in GRSMC 43.30-0.33 is shown in Figure 4 as a blue point. The position of this point on the x-axis is set by the ^{13}CO-derived volume-averaged density, while its y-axis position in the three subplots reflects the H_2CO measurements reported in Table 1.

Assuming that the thermal dominates the magnetic pressure ($\beta \gg 1$), we can fit σ_s from the model distributions in Figure 4. Using two different forms for the density distribution, and using only the τ measurements as a constraint, we derive the value of σ_s in Table 2 and seen in the bottom right panel of Figure 4.

Direct measurements of the Mach number from line-of-sight velocity dispersion measurements allow for further constraints on the distribution shape. Assuming a temperature $T = 10$ K, consistent with both the H_2CO and CO observations (Plume et al. 2004), the sound speed in molecular gas is $c_s = 0.19$ km s^{-1}. The gas is unlikely to be much colder; so this sound speed provides an upper limit on the Mach number. The observed line FWHM in G43.17 is 0.95 km s^{-1} for H_2CO and 1.7 km s^{-1} for ^{13}CO 1–0, so the three dimensional (3D) Mach number of the turbulence is (Schneider et al. 2013)

$$\mathcal{M}_{3D} \equiv 3^{1/2}\mathcal{M}_{1D} \approx \frac{3^{1/3}}{(8\ln 2)^{1/2}}\,\mathrm{FWHM}/c_s \qquad (6)$$

or $\mathcal{M}_{3D} = 3.8$–6.6, ranging from the H_2CO to the ^{13}CO width along the G43.17+0.01 line of sight. However, we note that the velocity dispersion for the whole cloud is larger.

Using the observed range of Mach numbers along the G43.17+0.01 line of sight, we can constrain b with Equation (3). Figure 5 shows the Mach number-b parameter space allowed by the observed volume density and H_2CO lines both with and without the Mach number constraint imposed. If we assume that the Mach number is approximately half way between the H_2CO- and CO-based measurements, with a dispersion that includes both, we can constrain $b > 0.56$ (see Table 2).

4.1.1. The Hopkins Distribution

As one possible alternative, we use the Hopkins (2013) density distribution,

$$P_V(\ln\rho)d\ln\rho = I_1(2\sqrt{\lambda u})e^{-(\lambda+u)}\lambda du, \qquad (7)$$

where $u \equiv \lambda/(1+T) - \ln(\rho/\rho_0)/T$ and $\lambda \equiv \sigma^2_{\ln\rho/\rho_0}/(2T^2)$ (Equation (5) in Hopkins 2013 modified such that ρ_0 is not assumed to be unity). The distribution is governed by a width $\sigma_s \equiv \sigma_{\ln\rho/\rho_0}$ and an "intermittency" parameter T that indicates the deviation of the distribution from lognormal. The intermittency parameter is described in Hopkins (2013) as a unitless parameter which increases with Mach number and is correlated with the strength of the deviations from the mean turbulent properties as a function of time. Its physical meaning beyond these simple correlations is as of yet poorly understood.

We use T values given the T–σ_s and T–$\mathcal{M}_C$ relations fitted to measurements from a series of simulations (Kowal & Lazarian 2007; Kritsuk et al. 2007; Schmidt et al. 2009; Federrath et al. 2010; Konstandin et al. 2012; Molina et al. 2012; Federrath 2013), where $\mathcal{M}_c$ is the compressive Mach number, e.g., $\mathcal{M}_c = b\mathcal{M}$. The values are given by

$$T(\sigma_s) = 0.25\ln(1 + 0.25\sigma_s^4\,(1 + T(\sigma_s))^{-6}). \qquad (8)$$

Equation (8) is a transcendental equation, so we use root-finding to determine T.

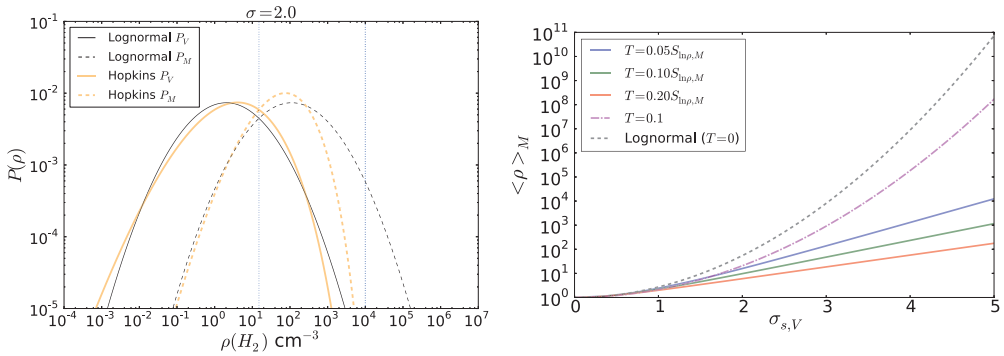

Figure 6. Left: example volume- and mass-weighted density distributions with $\sigma_s = 2.0$. The vertical dashed lines show $\rho = 15$ cm^{-3} and $\rho = 10^4$ cm^{-3}, approximately corresponding to the volume-weighted mean density $\langle\rho\rangle_V$ of GRSMC 43.30-0.33 from ^{13}CO and the H_2CO-derived density, respectively. Note that the peaks of the distributions do not correspond to their means, since the mean of the lognormal distribution depends on its variance. Right: the relationship between the mass-weighted mean density $\langle\rho\rangle_M$ and the width of the volume-weighted density PDF $P_V(\rho)$ for the lognormal distribution and different realizations of the Hopkins (2013) distribution with $\rho_0 = 1$. We show different forms of the T–σ relation using $T = c \cdot S_{\ln\rho,M}$, which is an approximation of Equation (8), and one example of T = constant. It is clear that, for a given distribution width, the Hopkins distribution always puts less mass at the highest densities than the lognormal distribution.

(A color version of this figure is available in the online journal.)

Assuming the same abundance as above, $X(H_2CO) = 10^{-8.5}$, the Hopkins distribution is incompatible with our observations for the T–σ relations considered in Hopkins (2013) and the other T values and relations explored in Figure 6(b). Figure 6(a) shows how the Hopkins and lognormal distributions differ; the Hopkins distribution is more sharply peaked and includes less gas above its peak density. The incompatibility with our observations arises because the Hopkins distribution produces lower mass-weighted densities than the lognormal.

However, the Hopkins distribution is compatible with our observations if a lower abundance is assumed. Using the Hopkins distribution with $X(H_2CO) = 10^{-9}$, we find $\sigma_s \sim 2.5$ (see Table 2). This value is compatible with the observed Mach numbers. Using the relation

$$b\mathcal{M} = \mathcal{M}_c \approx 20T \quad (9)$$

from Hopkins (2013) Figure 3, we can derive a lower limit $b > 0.7$. However, there is additional intrinsic uncertainty in the coefficient in Equation (9) that comes from fitting the relation to simulated data, and we have not accounted for this uncertainty.

The Hopkins distribution is compatible with our observations, but requires relatively extreme values of the standard deviation and b parameters. We explored a few alternative realizations of the Hopkins distribution's T–σ relation, with results shown in Figure 6. Independent of the form of the Hopkins distribution chosen, it is more restrictive than the lognormal distribution.

4.2. Discussion

The restrictions on σ_s and b using either the lognormal or Hopkins density distribution are indications that compressive forcing must be a significant, if not dominant, mode in this molecular cloud. However, there are no obvious signs of cloud–cloud collision or interaction with a supernova that might directly indicate what is driving the turbulence.

Most of the systematic uncertainties tend to require a *greater* b value, while we have already inferred a lower limit that is moderately higher than others have observed (Brunt 2010; Kainulainen et al. 2013). Temperatures in GMCs are typically 10–20 K, and we assumed 10 K: warmer temperatures increase the sound speed and therefore decrease the Mach number. If the cloud is warmer, the b values again must be higher to account for the measured σ_s. Magnetic fields similarly have the inverse effect of b on σ_s, with decreasing β requiring higher b for the same σ_s.

The only systematic that operates in the opposite direction is the abundance of o-H_2CO. Lower abundance shifts all curves in Figure 4 up and to the right, which decreases σ_s and therefore allows for a lower b for a fixed Mach number. However, abundances lower than $X = 10^{-9}$ are rarely observed except in Galactic cirrus clouds (Turner et al. 1989) and highly shocked regions such as the circumnuclear disk around Sgr A* (Pauls et al. 1996), so the measurements in Table 2 should bracket the allowed values. While we only explored two possible abundances in detail, note that the σ_s values derived from the lognormal distribution vary little over half-dex changes in abundance (Table 2), indicating that this measurement at least is robust to abundance assumptions.

We explore these caveats and others in more detail in the Appendix.

5. CONCLUSIONS

We demonstrate the use of a novel method of inferring parameters of the density PDF in a molecular cloud using H_2CO densitometry in conjunction with ^{13}CO-based estimates of total cloud mass. We have measured the standard deviation of the lognormal turbulence density distribution $1.5 < \sigma_s < 1.9$ and placed a lower limit on the compressiveness parameter $b > 0.4$. Both measurements are robust to the assumed cloud density, H_2CO abundance, and other assumptions.

Our data show evidence for compressively driven turbulence in a non-star-forming GMC. Since this cloud represents a typical molecular cloud, it is likely that compressive driving is a common feature of all molecular clouds.

This new method opens the possibility of investigating the drivers of turbulence more directly, e.g., by measuring the shape of the density PDF both within spiral arms and in the inter-arm regions. The main requirements for applying this technique are a moderately accurate measurement of the mean cloud density, which can easily be provided by ^{13}CO surveys such as the GRS, and a high signal-to-noise measurement of the 2 cm and 6 cm H_2CO lines.

A precise measurement of the Mach number of the cloud will allow *measurements* of b rather than the limits we have presented here. Investigations of the predicted observed velocity dispersion and line strengths in both H_2CO and ^{13}CO in

simulations of turbulent clouds should provide the details needed to take this next step.

Finally, the general approach of accounting for a density distribution by averaging over the contribution to the line profile at each density should be generally applicable to any molecular line observations as long as the lines are optically thin.

We thank Erik Rosolowsky and Ben Zeiger for useful discussions and comments that greatly improved the clarity of the paper. We thank the anonymous referee for a timely and constructive report that helped improve the paper. This publication makes use of molecular line data from the Boston University-FCRAO Galactic Ring Survey (GRS). The GRS is a joint project of Boston University and Five College Radio Astronomy Observatory, funded by the National Science Foundation under grants AST-9800334, AST-0098562, and AST-0100793. This research made use of Astropy, a community-developed core Python package for Astronomy (http://astropy.org; The Astropy Collaboration et al. 2013). It also made use of `pyspeckit`, an open source python-based package for spectroscopic data analysis (http://pyspeckit.readthedocs.org; Ginsburg & Mirocha 2011). The dendrogramming was performed using the python dendrogram package described at http://dendrograms.org. J.D. acknowledges the support of the NSF through the grant AST-0707713. C.F. is supported from the Australian Research Council with a Discovery Projects Fellowship (Grant DP110102191).

Facilities: GBT, Arecibo, FCRAO, CSO

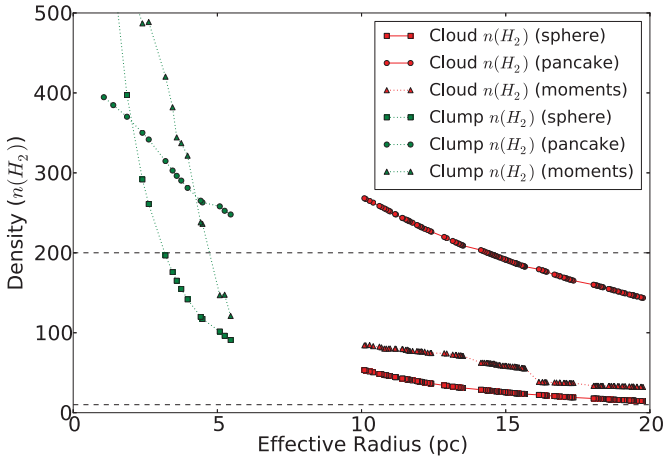

Figure 7. Results of a dendrogram analysis of the GRSMC 43.30-0.33 cloud and the northernmost ^{13}CO "clump" within that cloud. The data points represent successively higher (and therefore smaller) contours within the integrated ^{13}CO map. The shapes represent the three different methods for extracting the volume: squares assume spherical symmetry using the effective radius of the contour, which is proportional to the square root of the number of pixels. The circles do the same, but assume that the line-of-sight radius is 2 pc (i.e., smaller than the observed plane-of-the-sky dimensions). The triangles show the volume of an ellipsoid using the moments of the contoured pixels, with volume $V = 4/3\pi\, R_{\rm maj} R_{\rm min}^2$. The black dashed lines indicate the range of densities allowed in our fits.

(A color version of this figure is available in the online journal.)

APPENDIX

ASSUMPTIONS, CAVEATS, AND UNCERTAINTIES

We explore the various caveats and assumptions that have been treated above in more detail here.

The precise density measurements presented here are based on LVG approximations (Sobolev 1957) for the escape probability of line radiation from the cloud. This method is widely used but remains an approximation. In the case of H_2CO, it has been tested with a variety of codes (van der Tak et al. 2007; Henkel et al. 1983), but is subject to uncertainties in the velocity gradient and system geometry. However, in the case of the observations in this paper, the lines were observed in the optically thin regime, and the LVG approximation should not affect our results.

The collision rates of H_2CO with p-H_2, o-H_2, and He are estimated based on computer simulations of the particles. Troscompt et al. (2009) improved upon the measurements of Green (1991), bringing the typical collision rate uncertainty down from ∼50% in the He-based approximation to ∼10% using full models of ortho and para H_2. Wiesenfeld & Faure (2013) noted that the differences they observed from the Troscompt et al. (2009) results were <10%, indicating that the methods they use are at least convergent & self-consistent to within ∼30%. Zeiger & Darling (2010) reported the results of using modified collision rates assuming a 50% error and noted that the resulting errors in the H_2 density were, in the worst case, <0.3 dex. With the improved Troscompt et al. (2009) collision rates, the model uncertainties are no longer dominated by collision rate uncertainties.

Abundance remains a serious concern, as most studies of o-H_2CO abundance do not observe multiple transitions and therefore do not constrain the relative level populations. There are also general difficulties in measuring the absolute abundance of molecules, as the absolute column of H_2 is rarely known with high accuracy. Most abundance measurements are above $X_{\rm o\text{-}H_2CO} > 10^{-9}$ (Dickens & Irvine 1999; Liszt et al. 2006), except near Sgr A* (Pauls et al. 1996) and in Galactic Cirrus clouds (Turner et al. 1989; Turner 1993) where it is generally observed to have $10^{-10} < X_{\rm o\text{-}H_2CO} < 10^{-9}$. These measurements dictated the abundance boundaries we used in our analysis.

The ortho-to-para ratio of H_2 is a significant uncertainty in the models, since para-H_2 is more effective at "refrigerating" the H_2CO molecules. Values of the ortho-to-para ratio >1 favor lower densities by ∼0.3 dex, but we have used these lower densities in our analysis, and therefore our results are conservative. However, if the ortho-to-para ratio is in reality close to zero, the density PDF must be wider and b correspondingly higher.

The "covering factor" of foreground clouds in front of background illumination sources is, in general, a major concern when performing absorption measurements. For the clouds presented in this work, the absorbing region is much larger than the background, as evidenced by the two lines of sight with similar optical depth ratios. However, for more detailed studies of density variations, EVLA observations can and should be employed.

The single largest uncertainty is related to the mean properties of the GMC. While we have accounted for these uncertainties by adopting a very conservative range of values for the mean density (covering two orders of magnitude), it is not entirely clear how the mean density of the cloud should be computed for comparison to simulations and the analytic distributions. Since this is a foreground cloud lying in front of a rich portion of the galactic plane, the best mass estimates will always come from molecular line observations, and are therefore unlikely to be improved unless new wide-field CO observations are taken, e.g., with CCAT.

To validate our cloud mean density measurements, we have performed a dendrogram analysis (Rosolowsky et al. 2008) on

the integrated ^{13}CO map of the GRSMC 43.30-0.33 cloud. We perform the analysis both on the large-scale $r \sim 20$ pc cloud, tracking down to 10 pc scales, and then on the individual clump that is directly in front of W49. We show the cloud density, computed using the assumptions stated in the text to convert ^{13}CO luminosity to mass, for three different geometrical assumptions described in the caption of Figure 7. While the clump densities are potentially higher than we assumed in the analysis, they are probably not the appropriate numbers to compare to the simulations we have cited, which are generally simulating entire molecular clouds and measuring the density distribution within a large box.

REFERENCES

Aguirre, J. E., Ginsburg, A. G., Dunham, M. K., et al. 2011, ApJS, 192, 4
Brunt, C. M. 2010, A&A, 513, A67
Chabrier, G., & Hennebelle, P. 2010, ApJL, 725, L79
Cho, W., & Kim, J. 2011, MNRAS, 410, L8
Collins, D. C., Kritsuk, A. G., Padoan, P., et al. 2012, ApJ, 750, 13
Darling, J., & Zeiger, B. 2012, ApJL, 749, L33
Dickens, J. E., & Irvine, W. M. 1999, ApJ, 518, 733
Elmegreen, B. G. 2011, ApJ, 731, 61
Federrath, C. 2013, MNRAS, in press
Federrath, C., Chabrier, G., Schober, J., et al. 2011, PhRvL, 107, 114504
Federrath, C., & Klessen, R. S. 2012, ApJ, 761, 156
Federrath, C., & Klessen, R. S. 2013, ApJ, 763, 51
Federrath, C., Klessen, R. S., & Schmidt, W. 2008, ApJL, 688, L79
Federrath, C., Klessen, R. S., & Schmidt, W. 2009, ApJ, 692, 364
Federrath, C., Roman-Duval, J., Klessen, R. S., Schmidt, W., & Mac Low, M.-M. 2010, A&A, 512, A81
Ginsburg, A., Darling, J., Battersby, C., Zeiger, B., & Bally, J. 2011, ApJ, 736, 149
Ginsburg, A., Glenn, J., Rosolowsky, E., et al. 2013, ApJS, 208, 14
Ginsburg, A., & Mirocha, J. 2011, ascl soft, 9001
Glover, S. C. O., Federrath, C., Mac Low, M.-M., & Klessen, R. S. 2010, MNRAS, 404, 2
Green, S. 1991, ApJS, 76, 979
Henkel, C., Wilson, T. L., Walmsley, C. M., & Pauls, T. 1983, A&A, 127, 388
Hennebelle, P., & Chabrier, G. 2008, ApJ, 684, 395
Hennebelle, P., & Chabrier, G. 2009, ApJ, 702, 1428
Hennebelle, P., & Chabrier, G. 2011, ApJL, 743, L29
Hennebelle, P., & Chabrier, G. 2013, ApJ, 770, 150
Hopkins, P. F. 2012, MNRAS, 423, 2037
Hopkins, P. F. 2013, MNRAS, 430, 1653
Jackson, J. M., Rathborne, J. M., Shah, R. Y., et al. 2006, ApJS, 163, 145
Kainulainen, J., Federrath, C., & Henning, T. 2013, A&A, 553, 8
Kainulainen, J., & Tan, J. C. 2013, A&A, 549, 53
Klessen, R. S., Heitsch, F., & Mac Low, M.-M. 2000, ApJ, 535, 887
Konstandin, L., Girichidis, P., Federrath, C., & Klessen, R. S. 2012, ApJ, 761, 149
Kowal, G., & Lazarian, A. 2007, ApJL, 666, L69
Kritsuk, A. G., Norman, M. L., Padoan, P., & Wagner, R. 2007, ApJ, 665, 416
Kritsuk, A. G., Norman, M. L., & Wagner, R. 2011, ApJL, 727, L20
Krumholz, M. R., Dekel, A., & McKee, C. F. 2012, ApJ, 745, 69
Krumholz, M. R., & McKee, C. F. 2005, ApJ, 630, 250
Liszt, H. S., Lucas, R., & Pety, J. 2006, A&A, 448, 253
Mangum, J. G., & Wootten, A. 1993, ApJS, 89, 123
Mangum, J. G., Wootten, A., & Plambeck, R. L. 1993, ApJ, 409, 282
Molina, F. Z., Glover, S. C. O., Federrath, C., & Klessen, R. S. 2012, MNRAS, 423, 2680
Padoan, P., Haugbølle, T., & Nordlund, Å. 2012, ApJL, 759, L27
Padoan, P., & Nordlund, Å. 2002, ApJ, 576, 870
Padoan, P., & Nordlund, Å. 2011, ApJ, 730, 40
Padoan, P., Nordlund, Å., Kritsuk, A. G., Norman, M. L., & Li, P. S. 2007, ApJ, 661, 972
Patil, A., Huard, D., & Fonnesbeck, C. J. 2010, J. Stat. Softw., 35, 1
Pauls, T., Johnston, K. J., & Wilson, T. L. 1996, ApJ, 461, 223
Plume, R., Kaufman, M. J., Neufeld, D. A., et al. 2004, ApJ, 605, 247
Price, D. J., Federrath, C., & Brunt, C. M. 2011, ApJL, 727, L21
Roman-Duval, J., Jackson, J. M., Heyer, M., Rathborne, J., & Simon, R. 2010, ApJ, 723, 492
Roman-Duval, J., Jackson, J. M., Heyer, M., et al. 2009, ApJ, 699, 1153
Rosolowsky, E. W., Pineda, J. E., Kauffmann, J., & Goodman, A. A. 2008, ApJ, 679, 1338
Schmidt, W., Federrath, C., Hupp, M., Kern, S., & Niemeyer, J. C. 2009, A&A, 494, 127
Schneider, N., André, Ph., Könyves, V., et al. 2013, ApJL, 766, L17
Shetty, R., Glover, S. C., Dullemond, C. P., & Klessen, R. S. 2011a, MNRAS, 412, 1686
Shetty, R., Glover, S. C., Dullemond, C. P., et al. 2011b, MNRAS, 415, 3253
Simon, R., Jackson, J. M., Clemens, D. P., Bania, T. M., & Heyer, M. H. 2001, ApJ, 551, 747
Sobolev, V. V. 1957, SvA, 1, 678
Tang, X. D., Esimbek, J., Zhou, J. J., et al. 2013, A&A, 551, A28
The Astropy Collaboration, Robitaille, T. P., Tollerud, E. J., et al. 2013, A&A, 558, 33
Traficante, A., Calzoletti, L., Veneziani, M., et al. 2011, MNRAS, 416, 2932
Troscompt, N., Faure, A., Wiesenfeld, L., Ceccarelli, C., & Valiron, P. 2009, A&A, 493, 687
Turner, B. E. 1993, ApJ, 410, 140
Turner, B. E., Richard, L. J., & Xu, L.-P. 1989, ApJ, 344, 292
van der Tak, F. F. S., Black, J. H., Schöier, F. L., Jansen, D. J., & van Dishoeck, E. F. 2007, A&A, 468, 627
Wiesenfeld, L., & Faure, A. 2013, MNRAS, 432, 2573
Zeiger, B., & Darling, J. 2010, ApJ, 709, 386